Title: TiO_2-Bi_2O_3/$(BiO)_2CO_3$-reduced graphene oxide composite as an effective visible light photocatalyst for degradation of aqueous bisphenol A solutions

Authors: Gregor Žerjav, Petar Djinović, Albin Pintar

PII: S0920-5861(18)30111-1
DOI: https://doi.org/10.1016/j.cattod.2018.02.039
Reference: CATTOD 11264

To appear in: *Catalysis Today*

Received date: 3-11-2017
Revised date: 14-2-2018
Accepted date: 22-2-2018

Please cite this article as: Gregor Žerjav, Petar Djinović, Albin Pintar, TiO2-Bi2O3/(BiO)2CO3-reduced graphene oxide composite as an effective visible light photocatalyst for degradation of aqueous bisphenol A solutions, Catalysis Today https://doi.org/10.1016/j.cattod.2018.02.039

TiO_2-Bi_2O_3/$(BiO)_2CO_3$-reduced graphene oxide composite as an effective visible light photocatalyst for degradation of aqueous bisphenol A solutions

Gregor Žerjav*, Petar Djinović, Albin Pintar

Department for Environmental Sciences and Engineering, National Institute of Chemistry, Hajdrihova 19, SI-1001 Ljubljana, Slovenia.

*Corresponding author. Tel.: +386 1 47 60 249; fax: +386 1 47 60 460. *E-mail address:* gregor.zerjav@ki.si (G. Žerjav).

GRAPHICAL ABSTRACT

A novel multi-junction TBR photocatalyst (containing TiO_2, β-Bi_2O_3/$(BiO)_2CO_3$ and reduced graphene oxide) was prepared for oxidation of water dissolved bisphenol A (BPA) in advanced oxidation process under visible light illumination. The graphic shows band positions of each component before their close chemical contact as well as possible migration pathways of electrons and holes.

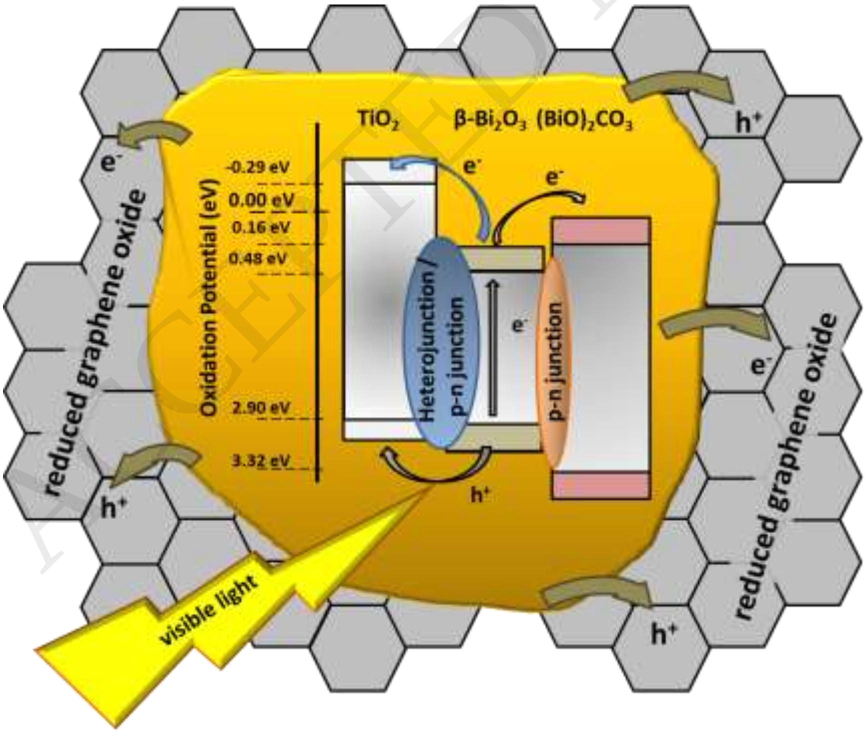

Highlights

- - Synthesis of multicomponent visible light active catalyst TiO_2-Bi_2O_3/$(BiO)_2CO_3$-rGO.
- - Bi_2O_3 act as photosensitizer for TiO_2 and $(BiO)_2CO_3$.
- - Heterojunction TiO_2/Bi_2O_3 enables the transfer of photo-generated holes.
- - P-n junction TiO_2/Bi_2O_3 enables the transfer of photo-generated electrons.
- - P-n junction Bi_2O_3/$(BiO)_2CO_3$ enables the transfer of photo-generated electrons.
- - Reduced graphene oxide (rGO) acts as a web for the percolation of charge carriers.

Abstract - TiO_2 nanorods (T) were combined with a narrow band gap semiconductor β-Bi_2O_3 (B) to form a heterojunction, which makes it possible for TiO_2 to become active as a photocatalyst also under visible light illumination. To further increase the photocatalytic activity of TiO_2+Bi_2O_3/$(BiO)_2CO_3$ (TB) composite, we used a hydrothermal procedure to link it with reduced graphene oxide (rGO). Structural, surface and electronic properties of the obtained catalysts were analyzed and correlated to their performance in photocatalytic oxidation of aqueous bisphenol A (BPA) solution conducted in a batch reactor under visible light illumination. XRD, FTIR, UV-Vis DR spectroscopy and photocurrent measurements of visible light illuminated TB composite catalyst clearly showed that (i) β-Bi_2O_3 acts as a photosensitizer for TiO_2 and $(BiO)_2CO_3$ present in the TB composite, (ii) holes (h^+) are photo-generated in valence band (VB) of β-Bi_2O_3 and due to the β-Bi_2O_3/TiO_2 heterojunction transferred into VB of TiO_2, (iii) p-n junction between β-Bi_2O_3 and TiO_2 allows the photo-generated electrons (e^-) in the conduction band (CB) of β-Bi_2O_3 to transfer to TiO_2, and (iv) p-n junction between β-Bi_2O_3 and $(BiO)_2CO_3$ allows the photo-generated electrons in the conduction band of β-Bi_2O_3 to transfer to $(BiO)_2CO_3$. This means that more charge carriers are available to participate in the catalytic visible-light triggered oxidation process for the degradation of organic pollutants dissolved in water. The highest photocurrent density was measured for multi-phase TBR (TB+rGO) composite, which indicates that visible-light generated charge carriers in TB composite are injected into the reduced graphene oxide. The latter acts as a web for charge carrier percolation and suppresses the recombination of electron-hole pairs, thus resulting in improved catalytic activity of TBR. The results of UV-Vis DR spectroscopy and photocurrent density measurements were entirely in line with the results of photocatalytic oxidation of water dissolved bisphenol A (BPA) in batch reactor under visible light illumination.

Keywords: visible light active catalyst; photocatalysis; TiO_2-Bi_2O_3/$(BiO)_2CO_3$-reduced graphene oxide composites; charge carriers migration; bisphenol A; reduced graphene oxide; TiO_2 nanorods; Bi_2O_3

1. Introduction

Due to its high photocatalytic activity, chemical stability, low cost and nontoxicity, titanium dioxide (TiO_2) holds several promising applications as a photocatalyst [1,2]. TiO_2 is one of the most suitable catalysts for heterogeneous photocatalytic oxidation of many organic pollutants present in aqueous medium due to its high-lying conduction band (CB) [3]. If a photocatalyst is illuminated by light with energy equal to, or greater than its band gap energy, an electron (e^-) in the valence band (VB) moves to the conduction band and leaves a hole (h^+) in the VB. Photo-generated holes and electrons can either (i) reduce and oxidize substrates adsorbed on the catalyst surface, or (ii) recombine with each other without any chemical reaction. Recombination of electrons and holes hinders the photocatalytic activity of catalysts. The overall efficiency of a photocatalyst is determined by its ability for (i) light absorption, (ii) electron-hole pair separation and migration, and (iii) efficiency of electron-hole pair utilization. The main drawbacks of TiO_2 as a photocatalyst are (i) band gap energy of 3.2 eV, which means that it can be excited only by ultraviolet (UVA) light ($\lambda<387$ nm), and (ii) fast electron-hole recombination.

In our previous study [4], we decorated anatase TiO_2 nanorods with reduced graphene oxide (rGO) to obtain TiO_2+rGO composite. Its structural, surface and electronic properties [5] revealed improved charge separation compared to pure TiO_2 due to the perfect matching of TiO_2 and rGO valence band maxima (VBM). The excited electrons of TiO_2 nanorods are injected into the CB of rGO due to band alignment, which minimizes the radiative electron-hole recombination. The rGO acts as a web for electron percolation, which significantly improves the electron migration [6,7]. It was also shown that it is critical to optimize the amount of rGO in the TiO_2+rGO composites to achieve the highest photocatalytic activity. Excess rGO can promote charge carrier recombination, thus decreasing the number of electrons and holes participating in a catalytic reaction [8,9]. Combining TiO_2 and rGO in a proper ratio presents a successful solution to hinder electron-hole recombination in TiO_2 and increase its photocatalytic activity [10-]. The downside of wide band gap energy of TiO_2 still remains, meaning that only UV light can trigger the excitation of electrons and formation of holes in such solids.

There are several options available to extend the light response of TiO_2 into the visible light region [13]. Coupling TiO_2 with a narrow band gap semiconductor (WO_3, In_2O_3, SnO_2, ...) is an effective way to improve the photostimulation and electron-hole separation. Bismuth based compounds were recently very effectively used to form a heterostructure and improve the optical response of TiO_2 ($BiOI/TiO_2$, $BiOCl/TiO_2$, $BiVO_4/TiO_2$, ...) [14-]. Bi_2O_3 has four different polymorphs, namely: monoclinic (α), tetragonal (β), body-centered cubic (γ) and face-centered cubic (δ), all exhibiting notably different light-matter interactions. The band gap energy of β-Bi_2O_3 (2.4 eV) is notably lower than that of α-Bi_2O_3 (2.8 eV), resulting in light absorption in a wider visible-light region. This manifests itself in β-Bi_2O_3 polymorph showing higher photocatalytic activity compared to α-Bi_2O_3 in the decomposition of methyl orange and *p*-chlorophenol under visible light illumination [17-]. Therefore, β-Bi_2O_3 appears as a promising candidate to form a heterojunction with TiO_2 and to use its photosensitizing effect to boost visible-light catalytic performance of TiO_2. The photocatalytic activity of pure β-Bi_2O_3 is poor because of the following unfavorable properties: (i) conduction band potential of Bi_2O_3 is too low to oxidize the surface O_2 to O_2^- through a fast single-electron reaction, resulting in fast electron-hole recombination [20], (ii) synthesis procedures of pure β-Bi_2O_3 generally produce very large particles and consequently low specific surface area materials (below 1 m^2/g) [21], and (iii) narrow band gap favors electron-hole recombination [22]. Several authors report that when β-Bi_2O_3 (p-type semiconductor) and $(BiO)_2CO_3$ (n-type semiconductor) are combined, a p-n heterojunction is formed which improves the photocatalytic activity of the composite. In this composite, the role of β-Bi_2O_3 is to act as a visible-light photosensitizer for $(BiO)_2CO_3$, which has a large band gap of 3.1 eV and is not photocatalytically active under visible light irradiation [23-]. The fast electron-hole recombination in β-Bi_2O_3 is hindered due to the transfer of photo-generated charge carriers to $(BiO)_2CO_3$, resulting in improved visible light catalytic activity of β-Bi_2O_3.

The aim of this work was to synthesize innovative multicomponent TiO_2-Bi_2O_3/$(BiO)_2CO_3$-rGO composites, where the role of: (i) Bi_2O_3 is to act as a visible light photosensitizer, (ii) appropriately positioned VB and CB of TiO_2 and $(BiO)_2CO_3$ act as selective sinks for photo-generated holes and electrons, respectively, and (iii) rGO acts as a web for the percolation of charge carriers that prolongs their separation and lifetime. We investigated how different combinations of TiO_2, β-Bi_2O_3, $(BiO)_2CO_3$ and rGO influence the structural and electronic properties of the synthesized composites, and how this manifests itself in the photocatalytic activity towards liquid-phase bisphenol A degradation. Bisphenol A (BPA) is an endocrine disrupting compound which finds widespread use in production of mostly packaging materials used every day [29]. These materials end as a waste in landfills, which usually leads to slow leaching of BPA into ground water. Therefore, due to environmental implications BPA was chosen as a model compound to test the photocatalytic activity of developed photocatalysts.

2. Experimental

2.1. Sample preparation

2.1.1. Synthesis of TiO_2 nanorods and graphene oxide

TiO_2 nanoparticles (DT-51, provided by Crystal Company) were hydrothermally treated to obtain TiO_2 nanorods, which were further calcined at 500°C in air for 2 h to obtain pure anatase TiO_2 nanorods (sample denoted as T). The details about the synthesis procedure are available in our previous work [4], where also the details about the synthesis procedure of graphene oxide are described (sample denoted as GO).

2.1.2. Synthesis of bismuth oxide (B) and TB composite

Solution combustion method was used to prepare pure bismuth oxide (sample denoted as B) and TiO_2-Bi_2O_3 composite (denoted as TB). To prepare Bi_2O_3, 2.9 g of $Bi(NO_3)_3{\cdot}5H_2O$ (Honeywell Fluka) and 1.4 g of citric acid monohydrate ($C_6H_8O_7{\cdot}H_2O$, Merck) were dissolved in 10 ml HNO_3 (Merck, 0.04 M) and stirred for 1 h. After complete dissolution, 0.04 g Pluronic® P-123 (Sigma-Aldrich) was added and stirred for 4 h. The obtained solution was transferred into a ceramic cup and placed inside an oven, where it was heated (temperature ramp 120°C/h) to 300°C for 24 h and left to cool down naturally to room temperature. In the case of TB composite synthesis, 0.58 g of $Bi(NO_3)_3{\cdot}5H_2O$ (Honeywell Fluka) and 0.29 g of citric acid monohydrate ($C_6H_8O_7{\cdot}H_2O$, Merck) were dissolved in 10 ml HNO_3 (Merck, 0.04 M) and stirred for 1 h. After that, 0.008 g of Pluronic® P-123 (Sigma-Aldrich) was added and stirred for another hour. Finally, 1 g of TiO_2 was added and stirred for 3 h. The suspension was transferred into a ceramic cup and placed inside an oven, where it was heated to 300°C for 24 h (temperature ramp 120°C/h) and allowed to cool down naturally to room temperature. The nominal composition of the TB composite was 0.25 g of Bi_2O_3 and 1 g of TiO_2.

2.1.3. Synthesis of TR, BR and TBR composites

Graphene oxide (0.05 g) was added to a mixture of absolute ethanol (Sigma Aldrich, 25 ml) and deionized water (50 ml). The amount of GO and ultimately rGO in the composites (4 wt. %) was chosen based on the experience gained during our previous study [4]. To exfoliate GO, the mixture was ultrasonicated for 2 h. Afterwards, 0.5 g of T, B or TB powders were added to the suspension which was ultrasonicated for another 2 h. The suspension was transferred into a 200 ml Teflon-lined autoclave and heated to 130°C for 4 h to hydrothermally reduce GO. The resulting products were recovered by centrifugation, washed with deionized water and dried in vacuum under cryogenic conditions. Samples were denoted as TR (TiO_2+rGO composite), BR (Bi_2O_3+rGO composite) and TBR (TB+rGO composite).

2.2. Characterization

Specific surface area, total pore volume and average pore size were determined using N_2 adsorption/desorption isotherms at -196°C (Micromeritics, model TriStar II 3020). The samples were before measurements degassed using a SmartPrep degasser (Micromeritics) in N_2 stream (Linde, purity 6.0) at elevated temperature (60 min at 90°C, followed by 240 min at 180°C). Brunauer, Emmett and Teller (BET) theory was applied in order to calculate the specific surface area of composites.

The morphology of synthesized materials was examined by field-emission scanning electron microscope (Carl Zeiss, model FE-SEM SUPRA 35VP), equipped with energy-dispersive detector (Oxford Instruments, model Inca 400).

X-ray powder diffraction (XRD) patterns of the catalysts were collected on PANanalytical X`pert PRO MPD diffractometer with Cu Kα1 radiation (1.54056 Å) in reflection geometry (scan range: 20-90° in increments of 0.034°). PDF standards from the International Centre for Diffraction Data (ICDD) were used for the identification of crystalline phases.

UV-Vis diffuse reflectance (UV-Vis DR) spectra were obtained at room temperature using Perkin-Elmer Lambda 35 UV-Vis spectrophotometer equipped with the RSA-PE-19M Praying Mantis accessory. White reflectance standard Spectralon© was used to record the background correction in the range of 200-700 nm.

FTIR measurements were recorded using the Perkin-Elmer FTIR spectrometer (model Frontier). Sample pellets were prepared by mixing 1 mg of the sample with 99 mg of KBr. They were ground in an agate mortar and pressed at 5 tonnes for 5 minutes. The spectra were collected in transmission mode using the MCT detector. The spectra shown are the average of 16 scans with a resolution of 4 cm^{-1} in the spectral range of 4000-450 cm^{-1}.

The photoresponse characteristics of prepared materials were evaluated by Metrohm Autolab PGSTAT30 potentiostat/galvanostat in a three-electrode electrochemical cell under intermittent visible light illumination (halogen lamp 150 W, λ_{max}= 520 nm, UV cut-off filter at 410 nm, Fig. S1) with 0 V bias potential (vs. SCE) in 0.1 M KOH aqueous solution. The filter was used to ensure that the working electrodes with deposited samples were illuminated only by visible light (Fig. S1 shows UV-vis DR spectra of the cut-off filter and the halogen lamp). Electrochemical impedance (EIS) spectra of prepared catalysts were obtained in the frequency range of 0.1-10^6 Hz; 0.1 M Na_2SO_4 was used as electrolyte. Screen-printed DropSens electrode (DropSens DRP-150) was used as working electrode, platinum as a counter electrode and calomel electrode (HANNA instruments HI5412) as a reference electrode. To prepare the working electrode, 10 μl of catalyst-ethanol suspension (12.5 mg of catalyst dispersed in 2.5 ml of absolute ethanol (Sigma Aldrich)) was dropped onto the surface of the screen-printed electrode and dried overnight at room temperature.

2.3. Photocatalytic oxidation experiments

A solution of bisphenol A (c_0=10 mg/l, BPA) in ultrapure water (18.2 MΩcm) was used for the photocatalytic experiments. The experiments were performed in a 250 ml batch slurry reactor (Lenz, model LF60, 250 ml) at atmospheric pressure, which was magnetically stirred (600 rpm) and thermostated at 20°C (Julabo, model F25/ME). Solution was purged with purified air during the whole experiment (45 l/h). The catalyst concentration used in all experiments was 125 mg/l. Ultrasonication was employed to suspend the catalyst before adding to the BPA solution. The suspension was kept in dark for 30 min ("dark" period, for establishing of the sorption process equilibrium) before illumination with halogen lamp (150 W, λ_{max}= 520 nm). An UV cut-off filter at 410 nm (Rosco E-Colour #226: U.V. filter) was used in all experiments to ensure that the catalysts tested were illuminated only by visible light (Fig. S1). The halogen lamp with UV filter was positioned in a water-cooled quartz jacket, which was immersed vertically in the center of the batch slurry reactor.

2.4. Analysis of end-product solutions

To determine temporal BPA conversions, 1.5 ml samples were withdrawn in 5-30 min intervals during the photolytic/photocatalytic runs. The samples were filtered through a 0.2 μm membrane filter and analyzed with an HPLC instrument (Thermo Scientific, model Spectra). Details about the HPLC analytical protocol can be found elsewhere [30]. By measuring the total organic carbon (TOC) content at the end of photocatalytic experiments using an instrument from Teledyne Tekmar (model Torch), the level of mineralization, i.e. the total amount of removed organic substances in aqueous-phase samples was determined.

3. Results and discussion

3.1. Catalyst characterization

3.1.1. SEM-EDX and N_2 physisorption analyses

SEM analysis was utilized to visualize the morphology of prepared solids (Fig. 1). A proper rod-like morphology was observed for the T sample (Fig. 1) with a length of 80±8 nm and a diameter of 10±2 nm. The morphology of pure Bi_2O_3 (B) was shaped as nanoplates with thickness of about 300 nm. Differences in the shape of B and T morphologies are expressed also in their BET surface areas (Table 1), where values of 4.7 and 105 m^2/g were calculated for samples B and T, respectively. Corresponding N_2 adsorption-desorption isotherms and BJH pore size distributions are present in Fig. 2. Low BET surface area of sample B was observed also by others [21]. After exfoliation and reduction of GO, a sheet-like morphology of sample rGO was obtained. SEM images (Fig. 1) reveal that after combining pure T with rGO or/and B, the nanorod-like structure of T is maintained, which implies that its morphology is not influenced by the subsequent hydrothermal GO reduction. In Fig. 3, SEM-EDX elemental mapping of TBR composite shows that bismuth is well distributed in the solid and decorated with titanium. Also, no segregation or clustering of T or B components could be noticed. Carbon was omitted from the results of SEM-EDX elemental mapping due to the fact that the samples were fixed with carbon tape, so we couldn’t reliably distinguish between carbon originating from the samples or carbon tape.

3.1.2. XRD analysis

Individual components (T, B and R) as well as their multi-phase composites were analyzed using XRD technique (Fig. 4). All diffraction lines observed in the XRD pattern of pure B correspond to tetragonal (β) Bi_2O_3 (JCPDS 00-27-0050). The peak at 9.8^o in the pure GO sample corresponds to the (002) interlayer spacing (d) of 0.90 nm, which matches very well with the value reported for graphene oxide [31]. In all other materials containing rGO, these are not visible, indicating successful reduction of GO to rGO. Analysis of pure T sample revealed only diffraction peaks characteristic for anatase TiO_2.

During analysis of composites, drastic changes related to β-Bi_2O_3 structure were observed. T appears to be not affected in any of the materials: it remains as anatase and its average scattering domain size changes negligibly (14, 15, 16 and 15 nm for pure T, TB, TR and TBR samples, respectively; see Table 1). In the TB composite, tetragonal β-Bi_2O_3 is present only as a minor phase (based on the intensity of its diffraction lines). The main crystalline bismuth containing component is bismuth carbonate ($(BiO)_2CO_3$, JCPDS 00-041-1488). In BR composite, tetragonal β-Bi_2O_3 is the prevailing phase in coexistence with bismuth carbonate ($(BiO)_2CO_3$). Based on these results, we can postulate that presence of anatase T strongly hinders formation of β-Bi_2O_3 during calcination step and the predominant bismuth-containing phase remains $(BiO)_2CO_3$. It is known that β-Bi_2O_3 cannot be produced by thermal decomposition of bismuth nitrate (more stable α- and γ-Bi_2O_3 polymorphs are produced in this case), but could be instead readily formed from bismuth carbonate [27]. Utilization of calcination temperatures higher than 300°C results in formation of α-Bi_2O_3 polymorph [27], which has a broader bandgap and consequently is unsuitable as a visible-light sensitizer of TiO_2. Also, β-Bi_2O_3 is not stable under the employed hydrothermal conditions used for GO reduction, leading to its partial conversion to $(BiO)_2CO_3$.

In the TBR composite, the only crystalline phase observed was anatase and only traces of β-Bi_2O_3 and $(BiO)_2CO_3$ were observed. Bismuth oxide is predominantly present in an amorphous form. This conclusion is supported by the fact that SEM-EDX elemental analysis shows bismuth content very close to the nominal one. Actual chemical compositions of TB and TBR composites calculated based on the SEM-EDX results are: 0.28 g Bi_2O_3 and 1 g TiO_2, and 0.21 g Bi_2O_3 and 1 g TiO_2, respectively.

3.1.3. FTIR analysis

Acquired FTIR spectra of prepared single-component catalysts are presented in Fig. 5a. The spectrum of sample T shows strong absorption in the range of 1000-450 cm^{-1}, which corresponds to lattice Ti-O-Ti vibrations. The broad band in the range of 3700-2500 cm^{-1} and a peak at 1640 cm^{-1} can be ascribed to stretching and bending vibrations of surface adsorbed hydroxyl groups and water, respectively [32].

The bands in the spectrum of GO sample appearing at 1050, 1220, 1414 and 1720 cm^{-1} are stretching vibrations of oxygen containing groups (alkoxy C-O, epoxy C-O, C-OH and carbonyl C=O). The broad band appearing between 3700 and 2500 cm^{-1} arises from stretching vibrations of surface hydroxyl (-OH) groups, while the band at 1626 cm^{-1} is attributed to C=C vibration of graphene oxide, thus confirming its sp^2 hybridized structure [33,34]. The latter is overlapping with water vibrations expected at 1630-1640 cm^{-1}.

In the B sample, bands below 700 cm^{-1} belong to the lattice Bi-O bond vibrations [35]. Strong absorption bands of CO_3^{2-} groups are observed at 1388 and 1440 cm^{-1}. These can be assigned to its anti-symmetric vibration ν_3 mode. At 845 cm^{-1}, an out of plane ν_2 bending mode characteristic of $(BiO)_2CO_3$ is observed. The broad absorption band between 3700 and 2700 cm^{-1} and at 1635 cm^{-1} can be attributed to the O-H stretching mode and bending modes of adsorbed water molecules, respectively [36].

Fig. 5b shows FTIR spectra of composites. In the TB composite, an intense Ti-O-Ti band (between 450 and 1000 cm^{-1}) was observed, which overwhelmed all other vibrations (those of bismuth oxide) expected in this region. Bands of hydroxyl groups and water (between 3700 and 2700 cm^{-1} and at 1625 cm^{-1}, respectively) and a doublet of carbonate bands at 1458 and 1392 cm^{-1} were also observed.

In the BR composite, Bi-O vibrations of bismuth oxide are observed below 750 cm^{-1}. Bands characteristic of carbonates (845, 1392 and 1458 cm^{-1}) confirm presence of $(BiO)_2CO_3$, which was identified also by XRD examination (Fig. 4). Vibrations from C=C sheets in rGO are confirmed by the band at 1625 cm^{-1}. Bands at 1110 and 1197 cm^{-1} suggest presence of C-O-C ether bonds, while the band at 1572 cm^{-1} is attributed to C=C aromatic stretching.

The FTIR spectrum of TR composite is dominated by Ti-O lattice vibrations below 1000 cm^{-1} and hydroxyl/water vibrations. The latter is overlapping with C=C vibration of graphene oxide. Several bands give away presence of carbonyl (1680 and 1718 cm^{-1}), carboxylic (1411 and 1240 cm^{-1}) and ether (1122 and 1060 cm^{-1}) functional groups.

Regarding the TBR composite, the FTIR spectrum is also dominated by lattice Ti-O and water/hydroxyl vibrations. The water band at 1633 cm^{-1} exhibits a notable shoulder at lower wavelengths, characteristic of C=C vibrations of reduced graphene oxide. Also, a band at 1688 cm^{-1} is apparent which can be attributed to surface carbonyl groups. Bands characteristic of ether functional groups also appear at 1110 and 1197 cm^{-1}. Bands characteristic of $(BiO)_2CO_3$ are weak, indicating this phase is poorly represented. This is in line with XRD analysis (Fig. 4), where no signal of crystalline $(BiO)_2CO_3$ could be observed.

Combined results of transmission FTIR and XRD analyses show that: (i) sample B contains mainly β-Bi_2O_3 with trace amounts of bismuth carbonate, TB composite consists mainly of $(BiO)_2CO_3$ and traces of β-Bi_2O_3, BR composite consists mainly of β-Bi_2O_3 and traces of $(BiO)_2CO_3$, whereas TBR composite contains amorphous Bi_2O_3 coexisting with traces of β-Bi_2O_3 and $(BiO)_2CO_3$ phases; (ii) different oxygen containing functional groups are still present in reduced graphene oxide after hydrothermal reduction: ether groups in presence of Bi_2O_3 and/or $(BiO)_2CO_3$ (BR composite), carbonyl groups in presence of TiO_2 (TR composite), and both ether and carbonyl groups in TBR composite.

3.1.4. UV-Vis DR analysis

Optical properties of prepared materials are presented in Fig. 6. Pure T sample shows strong absorption in the UV light region (400 to 200 nm) with a band gap of 3.28 eV, typical for anatase TiO_2 [37,38]. On the other hand, B sample shows strong visible light absorption and a band gap of 2.4 eV, typical for β-Bi_2O_3 [17]. The UV-Vis DR spectra of TB and TBR samples show strong absorption in the 550-200 nm range, indicating that prepared samples have a strong visible and UV light response, which is in contrast to pure T sample. There are two contributions observed in the acquired UV-Vis DR spectra: (i) the first one between 200 and 400 nm is related to absorption of UV light by T, and (ii) the second one above 500 nm corresponds to the absorption of visible light by β-Bi_2O_3. According to the literature [28] the band gap of $(BiO)_2CO_3$ is around 3.1-3.2 eV, meaning it can be activated by incident light with $\lambda<400$ nm. As a result, $(BiO)_2CO_3$ does not act as a visible light photosensitizer, but rather to accommodate photo-generated electrons originating from the conduction band of β-Bi_2O_3. The increasing background absorbance (above 400 nm in spectra of TR and above 550 nm in spectra of BR and TBR samples) is related to light absorption by rGO, which was also indicated by the color change of these samples that become dark grey after introduction of rGO (Fig. S2).

3.1.5. Photoelectrochemical measurements

The separation of photo-generated electron-hole pairs of all prepared solids was systematically tested by photocurrent (Fig. 7) and EIS (Fig. 8) measurements. The samples produced anodic photocurrent when the light was switched on, but only in the case of pure B sample as well as TB and TBR composites we can speak of a significant increase of the anodic current.

Concerning TB sample, photoelectrochemical measurements show that a heterojunction between T phase and β-Bi_2O_3, as well as between β-Bi_2O_3 and $(BiO)_2CO_3$ is formed. β-Bi_2O_3 works as a visible light photosensitizer for T phase.

The increase of the photocurrent density for TBR composite (for 30 % in the eighth illumination cycle in comparison to TB catalyst) clearly shows that rGO acts as a web for charge carriers percolation which prolongs their separation and consequently results in a higher photocurrent measured. High photocurrent density means that more charge carriers are available to produce hydroxyl radicals as active oxygen species, which can participate in the photocatalytic reaction [7,39].

The steady-state photocurrent density of pure B is approximately 20 and 30 fold lower in comparison to TB and TBR solids, respectively, which could be attributed to the low band gap energy of β-Bi_2O_3 and consequently fast electron-hole recombination.

The combination of B and rGO (BR sample) did not result in increased photocurrent density, which was also reported by other authors [40]. By looking into the CB position of rGO, it was observed that it lies at -0.08 eV *vs.* NHE, [41]. Considering that the CB of β-Bi_2O_3 lies at 0.16 eV (Fig. 10), it is too positive to enable transfer of photo-excited electrons from Bi_2O_3 to rGO. As a result, no increased photocurrent density is observed when rGO and β-Bi_2O_3 are coupled. On the other hand, the CB of TiO_2 lies at -0.29 eV, which is appropriate for the photo-generated electrons to migrate to rGO and thus segregate efficiently.

The photocurrent densities of T and TR samples are very low, which is attributed to their band gap energy (3.28 eV, see UV-Vis DR results, Fig. 6). The increase of photocurrent densities for these two samples is attributed to the fact that although UV cut-off filter was used, not all UV irradiation was eliminated (Fig. S1) which triggered the catalytic activity of TiO_2. Photocurrent density measurements show stable response for all materials in the last four out of eight subsequent illumination cycles. The decrease of photocurrent densities of some catalysts (B, BR and TB) during the first four illumination cycles is ascribed to the stabilization of the measuring system (i.e. dynamic equilibrium at the solid-liquid interface).

To further study charge transfer processes at the contact between electrode (surface of tested catalysts) and electrolyte (0.1 M Na_2SO_4), electrochemical impedance spectroscopy (EIS) was utilized. The results are present in the form of EIS Nyquist plots in Fig. 8, where the intermediate-frequency response is related to electron transport and transfer at the electrode (catalyst surface) - electrolyte (Na_2SO_4) interface [5]. The diameter of semicircles in the Nyquist plots reflects the charge transfer process, and the smaller diameter of semicircle presents the lower charge transfer resistance [42]. The TB sample and especially TBR catalyst have smaller semicircles in comparison to other tested catalysts. The semicircle diameter belonging to the TBR sample is smallest when rGO is present, indicating that the recombination of electron-hole pairs is further reduced after rGO addition. Nyquist plots of T and TB catalysts support the results of photocurrent measurements (Fig. 7) showing that there is a junction between TiO_2 and β-Bi_2O_3, as well as between β-Bi_2O_3 and $(BiO)_2CO_3$, resulting in more efficient charge carrier separation. Wide semicircle diameters of B and BR samples show that the low band gap energies of B and BR favor the recombination of electron-hole pairs.

Based on the results of UV-Vis DR, photocurrent and EIS measurements, we can predict that any meaningful photocatalytic activity of T based catalysts without B present can only be triggered by illumination with UV light. On the other hand, appreciable catalytic activity under visible light illumination is expected for TB and especially TBR composite. This postulation was tested in the subsequent experiments of photocatalytic BPA degradation.

3.2. Photocatalytic BPA oxidation

Fig. 9 shows BPA degradation curves obtained in the presence of synthesized materials. In the performed runs no leaching of catalyst constituents into the liquid phase was observed, as confirmed by means of ICP-OES analysis. The experiments were first conducted for 30 min without illumination (dark phase) to determine the extent of BPA adsorption on the catalyst surface. The obtained results show that the decrease of BPA concentration in the dark phase was below 3 %, which means than an influence of adsorption on measured data could be neglected. After 30 min, the BPA solution containing dispersed catalyst powder was illuminated with the same halogen lamp as used in the photocurrent measurements. The obtained c/c_0 vs. time dependencies were found to be reproducible with an error of conversions measured within ±1 %. The following decreasing order of BPA degradation was achieved: TBR > TB > TR > T > B > BR. This is completely in line with decreasing order of photocurrent density. As a result, we can state that the photocurrent density corresponds exactly to the photocatalytic activity and can be used as a reliable descriptor for predicting the photocatalytic activity. Degradation of BPA carried out over TBR and TB composites was significantly higher (94 and 80 % BPA conversions were achieved in 120 min, respectively) in comparison to all other solids examined in this work. This result is not surprising if we take into the consideration the highest photocurrent density measured under visible light illumination by TBR sample (Fig. 7), meaning that in the presence of this material more charge carriers are available to generate reactive OH· radicals which participate in photocatalytic oxidation reaction. Degradation of BPA when using TB composite was significantly higher in comparison to TR sample (34 % BPA conversion). The results show that in the TB composite a junction between T, β-Bi_2O_3 and $(BiO)_2CO_3$ was formed and that β-Bi_2O_3 is acting as a photosensitizer for T and $(BiO)_2CO_3$ under visible light illumination.

Combining T and rGO is an efficient way to boost photocatalytic activity of TiO_2 under UV light illumination, as rGO acts as a sink for electrons which prolongs their lifetime before recombination with holes [4]. Indeed, in our test we measured higher photocatalytic activity of TR sample compared to that of pure T (BPA conversions of 34 and 26 %, respectively).

Pure T exhibited some photocatalytic activity for BPA removal despite the fact that UV-Vis DR and photocurrent measurements suggest its photocatalytic activity under visible light as negligible. The observed behavior is likely triggered by some minority surface defect sites [43], which are able to absorb visible light and generate reactive OH radicals that ultimately participate in the catalytic reaction.

Although pure B sample exhibits the highest absorption of visible light among all tested samples (Fig. 6), its low BET specific surface area, especially narrow band gap and inappropriate position of the conduction band promote recombination of electron-hole pairs which in turn ultimately hinders its photocatalytic activity. The BR composite shows lower photocatalytic activity compared to pure β-Bi_2O_3, very likely as a result of its partial transformation to $(BiO)_2CO_3$. The conduction band of $(BiO)_2CO_3$ is 3.1 eV [28]; it is too wide to allow visible light absorption, thus making this material inappropriate as a visible light driven photocatalyst.

At the end of each BPA degradation run, TOC value of the reaction solution was measured in order to evaluate the extent of BPA mineralization. The results of TOC measurements (Table 2) are in good correlation with the obtained BPA conversions (Fig. 9): the highest degree of BPA mineralization was achieved over TB and TBR composites. CHNS elemental analysis was further performed on fresh and spent catalyst samples (Table 2) to determine the true TOC removal (TOC_m) and TOC_a values corresponding to carbon-containing species accumulated on the catalyst surface, which constitute the TOC_R value. The listed results reveal that the amount of carbon deposited on spent samples was higher than on fresh solids, which is a sign that BPA and/or partially oxidized BPA degradation products adsorb on the catalyst surface. This can be most probably attributed to high BET specific surface area of T sample (or T component in TB composite).

The BPA degradation rates in the second half of performed oxidation runs (Fig. 9, t > 60 min) conducted in the presence of B, T, TR and BR catalysts are zero ($d(C/C_{0,BPA})/dt=0$), which is a sign that these catalysts were deactivated by adsorption of partially oxidized reaction intermediates onto the catalyst surface that block active sites. CHNS elemental analysis results of fresh and spent B catalyst also show that TOC_a is higher than TOC_m (1.4 and 2.6 %, respectively, Table 2), revealing that the predominant pathway of BPA removal from the liquid phase over this catalyst is actually adsorption of partially oxidized reaction intermediates. The same is true for T sample, as TOC_a and TOC_m values of 4 and 7 % were calculated.

In the case of TB composite, the results of CHNS elemental analysis clearly show that the main pathway of BPA removal is photocatalytic oxidation (43 % TOC_m) and not adsorption of partially oxidized reaction intermediates (8 % TOC_a). Composites containing rGO were not subjected to CHNS elemental analysis, because rGO influences the measurements which could lead to false conclusions.

We performed FTIR and XRD analyses of spent TB and TBR catalysts. XRD results (Fig. S3) showed that no changes of the crystalline components (TiO_2, β-Bi_2O_3 and $(BiO)_2CO_3$) occur during photocatalytic runs, indicating that all these crystalline phases are stable under the employed reaction conditions. FTIR results showed an increase of band intensity at 1572 and 1688 cm^{-1} in spent TBR catalyst. These vibrations occur due to the presence of C=C bonds in aromatic compounds as well as of carbonyl group containing species, respectively, indicating that carbonaceous deposits were formed during photocatalytic oxidation of BPA, or during oxidation of the rGO component. These deposits are not observed in spent TB catalyst, where the rGO component is absent. We tested also the reuse of TBR catalyst for BPA degradation. The results of the second run (Fig. S5) show that conversion of BPA was 5 % lower in comparison to the first run (94 and 89 %, respectively). The TOC removal was also lower (60 vs. 50 % for the first and second run, respectively). The decrease of TBR catalyst activity was noted in further oxidation cycles (Fig. S5). The XRD and FTIR measurements performed on spent TBR sample show that the catalyst is structurally stable under employed reaction conditions, so deactivation is likely related to adsorption of organics.

3.3. Proposed charge carrier migration cascade

The valence band edge (E_{VB}) and the conduction band edge (E_{CB}) of T and B catalysts were calculated accordingly to the Mulliken electronegativity theory [44,45]:

$$E_{VB} = X - E^{e} + 0.5 * \ E_{BG} \tag{1}$$

where E_{VB} is the VB edge potential, X is the electronegativity of the semiconductor, E^{e} is the energy of free electrons on the hydrogen scale (about 4.5 eV) and E_{BG} is the corresponding band gap energy of the semiconductor. The conduction band edge can be calculated as follows:

$$E_{CB} = E_{VB} - E_{BG} \tag{2}$$

On the basis of UV-Vis DR measurements (Fig. 6), the E_{BG} values of T and B catalysts are equal to 3.2 and 2.45 eV, respectively. Accordingly to Xu and Schoonen [45], their corresponding electronegativities are 5.81 and 6.21 eV, respectively. Consequently, calculated E_{VB} and E_{CB} are 2.91 and -0.29 eV for pure T, and 2.93 and 0.48 eV for B catalyst. The low conduction band edge of B catalyst (0.48 eV) cannot provide sufficiently negative potential for the photo-excited electrons to scavenge the adsorbed O_2 ($E^{o}(O_2/O_2^{\cdot-})$=-0.33 V vs. NHE and $E^{o}(O_2/HO_2^{\cdot})$=-0.05 V vs. NHE) [20,46]. This in turn causes fast recombination of photo-excited electron-hole pairs. This property of B catalyst was well displayed by the results of photocurrent and EIS measurements (Figs. 7 and 8) and photocatalytic BPA degradation tests (Fig. 9).

Based on the above presented results and discussion, a plausible charge carrier migration cascade for TB composite catalyst is illustrated in Fig. 10a. In this material, a heterojunction between TiO_2 (T) and β-Bi_2O_3 is formed which supports the “transfer” of photo-generated holes

(h^+) from VB of β-Bi_2O_3 to upper lying VB of T. The holes can react with hydroxide ions to form hydroxyl radicals (reaction 3), which actively participate in the degradation of water dissolved BPA molecules:

$$OH^- + h^+ \rightarrow OH^\cdot \tag{3}$$

The electrons (e^-) in the CB of β-Bi_2O_3 can react accordingly to reactions 4 and 5, which are pH dependent [47-]:

$$O_2 + 2H^+ + 2e^- \rightarrow H_2O_2 \qquad E^O = +0.682\,V\ (vs\ NHE) \tag{4}$$

$$O_2 + 4H^+ + 4e^- \rightarrow 2H_2O \qquad E^O = +1.23\,V\ (vs\ NHE) \tag{5}$$

The VB edge of β-Bi_2O_3 is positioned lower than the VB edge of TiO_2 [50], thus making the transfer of h^+ in this direction thermodynamically possible. Photo-generated h^+ in the VB of β-Bi_2O_3 as well as those transferred into the VB of T can react with H_2O or OH^- adsorbed on the surface of both components.

On the other hand, recombination of photo-generated electron-hole pairs can be effectively suppressed when a p-n junction is formed between tightly chemically bonded n-type semiconductor TiO_2 and p-type semiconductor Bi_2O_3 [51]. Before contact, the Fermi level of p-type β-Bi_2O_3 is more negative than that of n-type TiO_2 due to its smaller work function [52,53]. When a chemical contact is established between TiO_2 and Bi_2O_3, the Fermi level of β-Bi_2O_3 is moved up and the Fermi level of TiO_2 is moved down until an equilibrium state of Fermi levels (E_F) and inner electric field is formed at the interface between TiO_2 and β-Bi_2O_3 [54,55]. As shown in Fig. 10b, photo-generated e^- at the CB of β-Bi_2O_3 can migrate to TiO_2, since only β-Bi_2O_3 can produce photo-generated charge carriers under visible light irradiation. Both XRD and FTIR analyses confirmed $(BiO)_2CO_3$ in the TB catalyst. Accordingly to the literature, the band gap of $(BiO)_2CO_3$ is around 3.1 eV [28] and the values of E_{VB} and E_{CB} calculated by means of Eqs. 2 and 3 are 0.16 and 3.32 eV, respectively. The energy band structures of β-Bi_2O_3 and $(BiO)_2CO_3$ which are not in a contact, are illustrated in Fig. 10a. Comparison of the band positions shows that in this case the band structure is unfavorable for the separation of photo-generated electron-hole pairs. However, when a contact between β-Bi_2O_3 and $(BiO)_2CO_3$ is established, a p-n junction is formed since β-Bi_2O_3 is a p-type semiconductor, and $(BiO)_2CO_3$ is known as a n-type semiconductor. Because of the p-n junction the Fermi levels (E_F) of semiconductors will reach an equilibrium state and a newly formed energy band structure is formed as shown in Fig. 10c. It is necessary to point out that the adjusted energy band structure is favorable for the separation of visible light generated electrons from β-Bi_2O_3 to $(BiO)_2CO_3$ due to the effect of inner electric field analogous to other kinds of p-n junctions [25,27,28]. As demonstrated before (Figs. 7 and 9), the improved charge carrier separation in TB composite resulted in higher photocurrent during electrochemical measurements and enhanced activity in the process of photocatalytic BPA oxidation. To conclude, the role of β-Bi_2O_3 in TB composite is to act as a visible light photosensitizer as the band gap energies of both T and $(BiO)_2CO_3$ are inappropriate for visible light absorption.

In the TBR composite, the photo-generated charge carriers in TB are injected to the rGO that acts as a web for their percolation. The migration of charge carriers is significantly improved, meaning that also the recombination of electron-hole pairs is additionally hindered when compared to the TB composite (see, for instance, results of photocurrent measurements displayed in Fig. 7 and EIS measurements depicted in Fig. 8). The extended lifetime of photo-generated charge carriers and consequently enhanced formation of reactive radical species ($OH\cdot$ and $O_2\cdot$ can be formed from water on TiO_2 via the one hole reaction, or on β-Bi_2O_3 and $(BiO)_2CO_3$ via slower two electron reactions, see Eqs. 4 and 5) due to percolation by rGO is well expressed by the results of photocatalytic BPA degradation tests (Fig. 9), where the highest degradation and mineralization of BPA were achieved in the presence of TBR composite.

4. Conclusions

Several composites containing TiO_2, bismuth oxide and bismuth carbonate as well as rGO were synthesized, characterized and tested for photocatalytic activity in BPA degradation. The morphology of TiO_2 nanorods was not influenced by the synthesis conditions employed in the subsequent preparation procedure of TB and TBR composites. However, β-Bi_2O_3 was transformed into $(BiO)_2CO_3$ at different extents. In all bismuth containing composites, light absorption was shifted into the visible range indicating its appropriateness to act as a photosensitizer for TiO_2. In the TB composite, a heterojunction between β-Bi_2O_3 and TiO_2 is formed, which allows the transfer of visible light photo-generated h^+ from the VB of β-Bi_2O_3 to upper lying VB of TiO_2. In addition, a p-n junction between TiO_2 and β-Bi_2O_3 can be formed enabling the transfer of photo-generated e^- in CB of β-Bi_2O_3 to CB of TiO_2. Also, $(BiO)_2CO_3$ that appears in the TB composite forms a p-n junction with β-Bi_2O_3, which enables the transfer of photo-generated e^- in β-Bi_2O_3 to $(BiO)_2CO_3$. Consequently, recombination of electron-hole pairs in the TB composite is significantly hindered, which was confirmed by photoelectrochemical measurements. The photocurrent triggered by visible light in B and BR composite catalysts was low, which is attributed to the narrow band gap of β-Bi_2O_3 favoring the recombination of electron-hole pairs. The function of rGO in TBR composite catalyst is to act as a web for the percolation of charge carriers which prolongs their lifetime, making more charge carriers available for utilization in catalytic reactions, as compared to TB composite. This was confirmed by photoelectrochemical measurements, as 4 wt. % rGO content evidently improved the photocurrent density. The TBR composite exhibited the highest extent of BPA degradation and mineralization among all tested catalysts. XRD analysis of the spent TBR catalyst showed that it is structurally stable, hence deactivation observed during the catalyst reuse was likely caused by accumulation of carbonaceous species and/or oxidation of rGO.

Acknowledgements - The authors gratefully acknowledge the Slovenian Research Agency (ARRS) for financial support through Research Program No. P2-0150. Mr. Janvit Teržan and

Mr. Kristijan Lorber are kindly acknowledged for help with transmission FTIR measurements and photocatalytic tests.

References

1 K. Hashimoto, H. Irie, A. Fujishima, Jpn. J. Appl. Phys. 12 (2005) 8269-8285.

2 M. Ge, C. Cao, J. Huang, S. Li, Z. Chen, K.-Q. Zhang, S. S. Al-Deyab, Y. Lai, J. Mater. Chem. A 4 (2016) 6772-6801.

3 J. Zhang, Q. Xu, Z. Feng, M. Li, C. Li, Angew. Chem. 9 (2008) 1766-1769.

4 G. Žerjav, M.S. Arshad, P. Djinović, I. Junkar, J. Kovač, J. Zavašnik, A. Pintar, Nanoscale, 9 (2017) 4578-4592.

5 F.-X. Xiao, J. Miao, B. Liu, J. Am. Chem. Soc. 136 (2014) 1559-1569.

6 A. Adán-Más, D. Wei, Nanomaterials, 3 (2013) 325-356.

7 P. Dong, Y. Wang, L. Guo, B. Liu, S. Xin, J. Zhang, Y. Shi, W. Zeng, S. Yin, Nanoscale 4 (2012) 4641-4649.

8 G.P. Sing, K.M. Shrestha, A. Nepal, K.J. Klabunde, C.M. Sorensen, Nanotechology 26 (2014) 265701-265712.

9 Y. Liu, RSC Adv. 4 (2014) 36040-36045.

10 N. Zhang, M.-Q. Yang, S. Liu, Y. Sun, Y.-J. Xu, Chem. Rev. 18 (2015) 10307-10377.

11 M.-Q. Yang, N. Zhang, M. Pagliaro, Y.-J. Xu, Chem. Soc. Rev. 43 (2014) 8240-8254.

12 N. Zhang,Y. Zhang, Y.-J. Xu, Nanoscale 4 (2012) 5792-5813.

13 S. Malato, P. Fernandez-Ibanez, M.I. Maldonato, M. Blanco, W. Gernjak, Catal. Today, 147 (2009) 1-59.

14 X. Zhang, L.Z. Zhang, T.F. Xie, D.J. Wang, J. Phys. Chem. C 113 (2009) 7371-7378.

15 F. Duo, Y. Wang, C. Fan, X. Mao, X. Zhang, Y. Wang, J. Liu, Mater. Charact. 99 (2015) 8-16.

16 L. Zhang, G. Tann, S. Wei, H. Ren, A. Xia, Y. Luo, Ceram. Int. 39 (2013) 8597-8604.

17 H. Cheng, B. Huang, J. Lu, Z. Wang, B. Xu, X. Qin, X. Zhang, Y. Dai, Phys. Chem. Chem. Phys. 12 (2010) 15468-15475.

18 H.W. Kim, Thin Solid Films 516 (2008) 3665-3668.

19 J. Hou, C. Yang, Z. Wang, W. Zhou, S. Jiao, H. Zhu, Appl. Catal. B 142-143 (2013) 504-511.

20 H.Y. Jiang, K. Cheng, J. Lin, Phys. Chem. Chem. Phys. 14 (2012) 12114-12121.

21 A. Hameed, T. Montini, V. Gombac, P. Fornasiero, J. Am. Chem. Soc. 130 (2008) 9658-9659.

22 L. Li, X. Huang, T. Hu, J. Wang, W. Zhang, J. Zhang, New. J. Chem 38 (2014) 5293-5302.

23 P. Wang, L. Xu, Y. Ao, C. Wang, J. Colloid. Interf. Sci. 495 (2017) 122-129.

24 Y. Bian, Y. Ma, Y, Shang, P. Tan, J. Pan, Appl. Surf. Sci. (2017) https://doi.org/10.1016/j.apsusc.2017.06.063.

25 G. Cai, L. Xu, B. Wei, J. Che, H. Gao, W. Sun, Mater. Lett. 120 (2014) 1-4.

26 Y. Huang, W. Fan, B. Long, H. Li, F. Zhao, Z. Liu, Y. Tong, H. Ji, Appl. Catal. B 185 (2016) 68-76.

27 R. Hu, X. Xiao, S. Tu, X. Zuo, J. Nan, Appl. Catal. B 163 (2015) 510-519.

28 G. Zhu, Y. Liu, M. Hojamberdiev, J. Han, J. Rodríguez, S. A. Bilmes, P. Liu, New J. Chem. 39 (2015) 9557-9568.

29 C.A. Staples, P.B. Dome, G.M. Klecka, S.T. Oblock, L.R. Harris, Chemosphere 36 (1998) 2149-2173.

30 B. Erjavec, T. Tišler, R. Kaplan, A. Pintar, Ind. Eng. Chem. Res. 52 (2013) 12559-12566.

31 G.P. Sing, K.M. Shrestha, A. Nepal, K.J. Klabunde, C.M. Sorensen, Nanotechnology, 26 (2014) 265701-265712.

32 B. Erjavec, R. Kaplan, A. Pintar, Catal. Today 241 (2015) 15-24.

33 P.T.N. Nguyen, C. Salim, W. Kurniawan, H. Hinode, Catal. Today 230 (2014) 166-173.

34 D. Liang, C. Cui, H. Hu, Y. Wang, S. Xu, B. Ying, P. Li, B. Lu, H. Shen, J. Alloy. Compd. 582 (2014) 236-240.

35 L. Liu, J. Jiang, S. Jin, Z. Xia, M. Tang, CrystEngComm 13 (2011) 2529-2532.

36 J.Z. Marinho, L.M. Santos, L.R. Macario, E. Longo, A.E.H. Machado, A.O.T. Patrocinio, R.C. Lima, J. Braz. Chem. Soc. 26 (2015) 498-505.

37 J. Zhang, P. Zhou, J. Liu, J. Yu, Phys. Chem. Chem. Phys. 16 (2014) 20382-20386.

38 C. Dette, M.A. Pérez-Osorio, C.S. Kley, P. Punke, C.E. Patrick, P. Jacobson, F. Giustino, S.J. Jung, K. Kern, Nano Lett. 14 (2014) 6533-6538.

39 A. Adán-Más, D. Wei, Nanomaterials 3 (2013) 325-356.

40 X. Liu, L. Pan, T. Lv, Z. Sun, C.Q. Sun, J. Colloid Interface Sci. 408 (2013) 145-150.

41 S. Singha, N. Khare, RSC Adv. 5 (2015) 96562-96572.

42 X. T. Wang, C. H. Liow, D. P. Qi, B. W. Zhu,W. R. Leow, H. Wang, C. Xue, X. D. Chen, S. Z. Li, Adv.Mater. 26 (2014) 3506–3512.

43 W. Göpel, A. Anderson, D. Frankel, M. Jaehnig, K. Phillips, J.A. Schäfer, G. Rocker, Surf. Sci. 139 (1984) 333-346.

44 M.A. Butler, D.S. Ginley, J. Electrochem. Soc. 125 (1987) 228-232.

45 Y. Xu, M.A.A. Schoonen, Am. Mineral. 85 (2000) 543-556.

46 D.T. Sawyer, J.S. Valentine, Acc. Chem. Res. 14 (1981) 393-400.

47 R. Abe, H. Takami, N. Murani, B. Ohtani, J. Am. Chem. Soc. 130 2008 7780-7781.

48 G. Liu, L. Wan, C. Sun, X. Wang, Z. Chen, S.C. Smith, H.M. Cheng, G.Q. Lu, Chem. Mater. 21 (2009) 1266-1274.

49 P.Y. Ayekoe, D. Robert, D.L. Gone, Environ. Chem. Lett. 14 (2016) 387-393.

50 D. Beydoun, R. Amal, G. Low, S. McEvoy, J. Mol. Catal. A 180 (2002) 193-200.

51 Y. Huang, Y. Wei, J. Wang, D. Luo, L. Fan, J. Wu, Appl. Surf. Sci. 423 (2017) 119-130.

52 S. Yi, X. Yue, D. Xu, Z. Liu, F. Zhao, D. Wangab, Y. Lin, New J. Chem. 39 (2015) 2917-2924.

53 N. Wei, H. Cui, C. Wang, G. Zhang, Q. Song, W. Sun, X. Song, M. Sun, J. Tian, J. Am. Ceram. Soc. 100 (2017) 1339-1349.

54 Z. Zhang, C. Shao, X. Li, C. Wang, M. Zhang, Y. Liu, ACS Appl. Mater. Interfaces 2 (2010) 2915-2923.

55 G. Dai, J. Yu, G. Liu, J. Phys. Chem. C 115 (2011) 7339–7346.

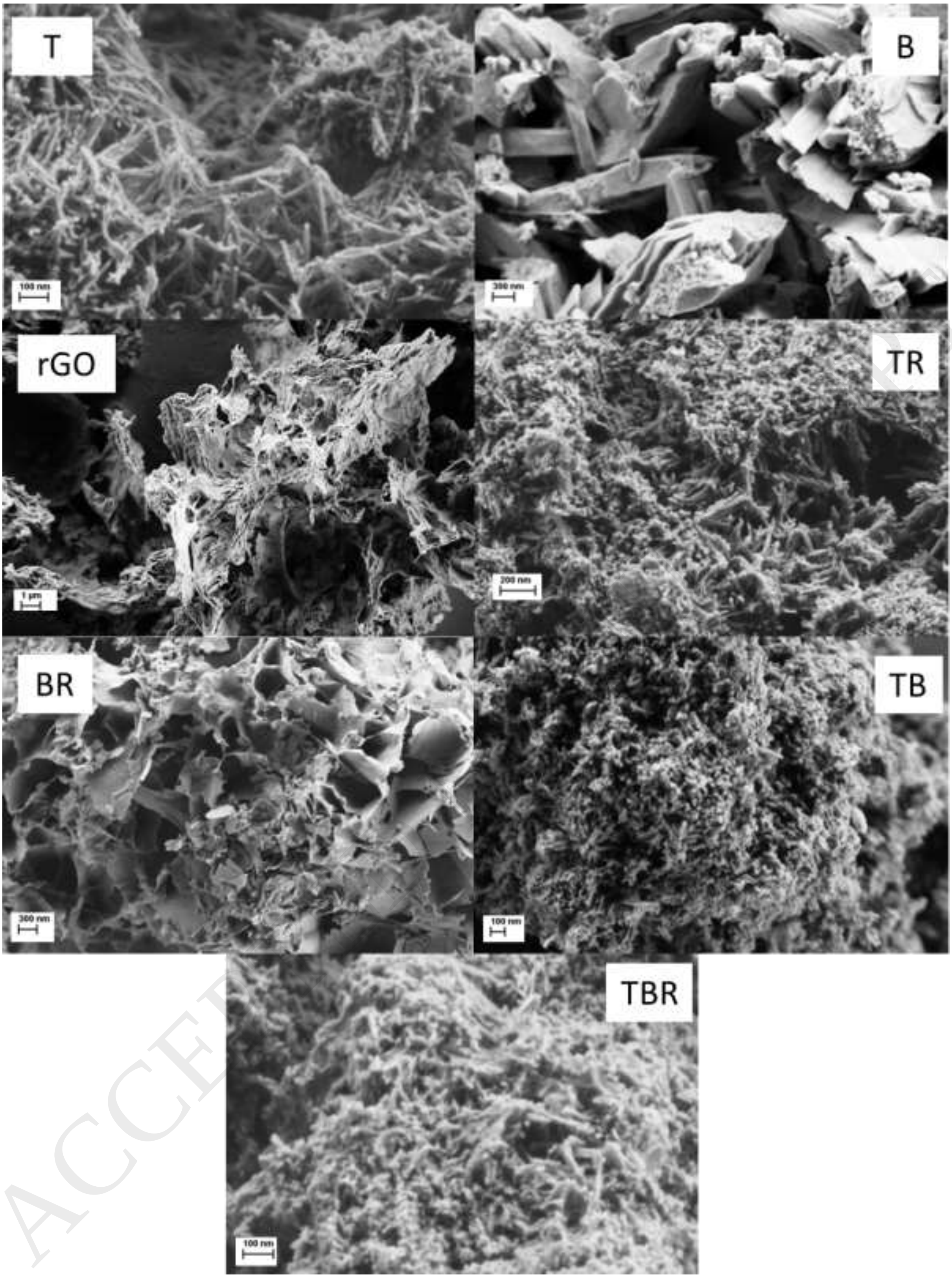

Fig. 1. SEM images of prepared catalysts.

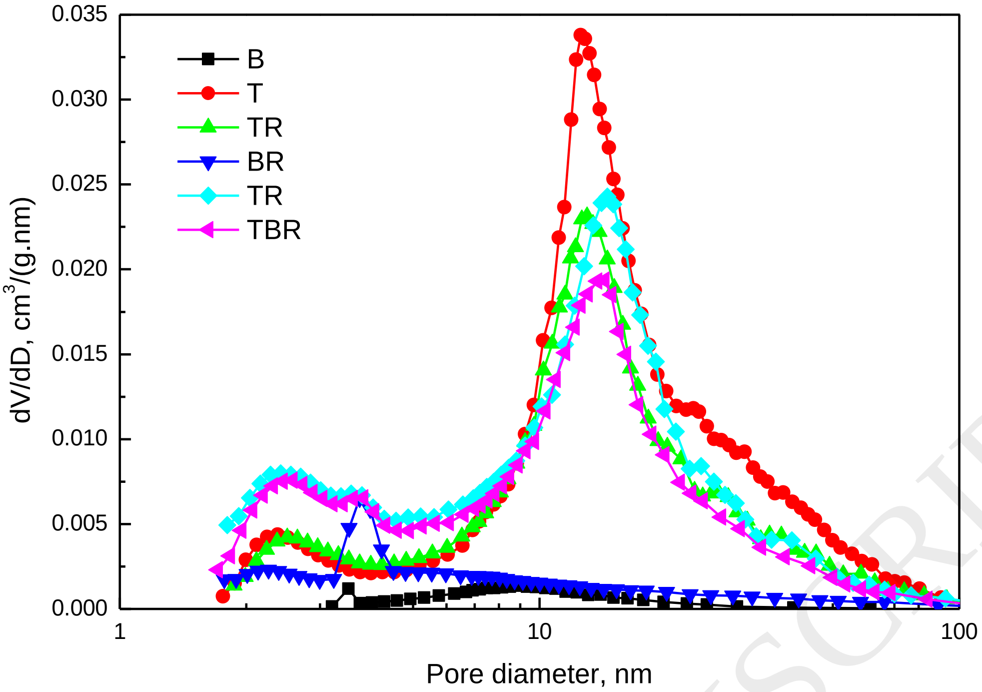

Fig. 2. a) N_2 adsorption-desorption isotherms and b) BJH pore size distribution of synthesized catalysts.

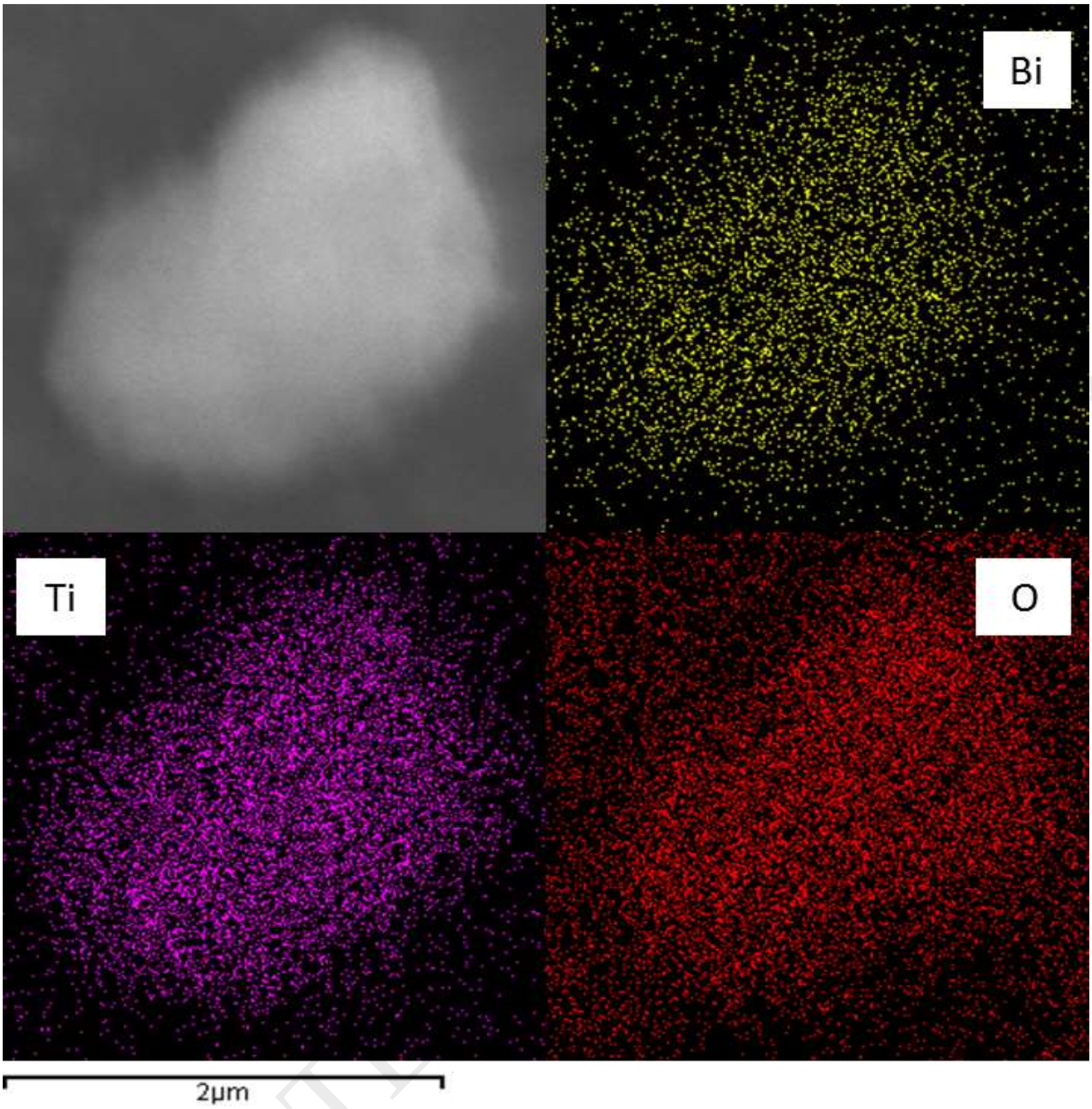

Fig. 3. SEM-EDX mapping of TBR sample.

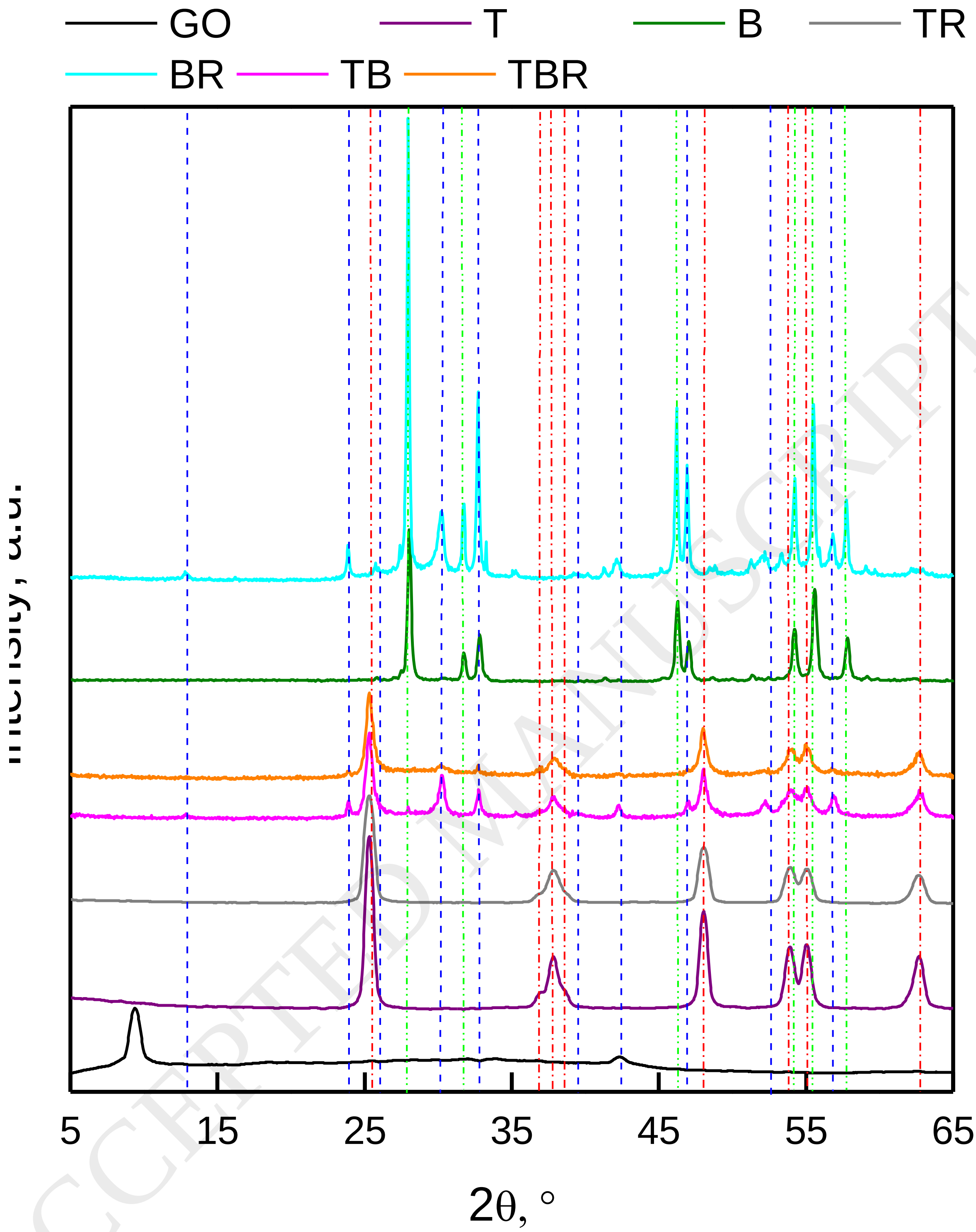

Fig. 4. XRD patterns of prepared single-phase catalysts as well as multi-phase composites. Vertical blue lines indicate most intensive reflections of $(BiO)_2CO_3$ (JCPDS 00-041-1488), while red and green lines indicate reflections of anatase TiO_2 (JCPDS 00-021-1272) and β-Bi_2O_3 (JCPDS 00-027-0050), respectively.

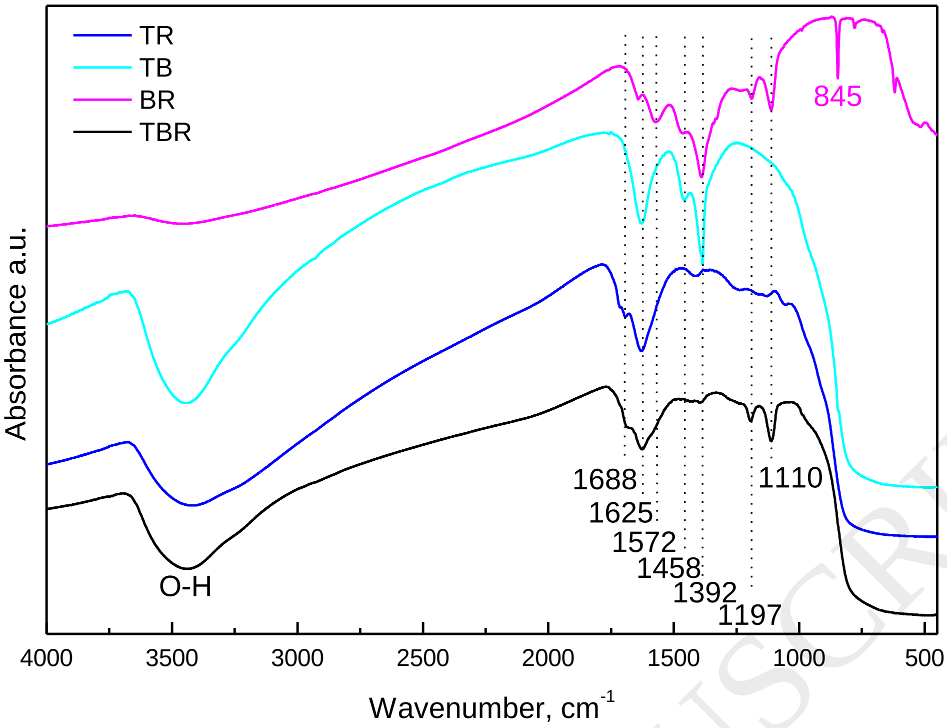

Fig. 5. FTIR spectra of a) pure T, B and G samples, and b) their multi-phase composite.

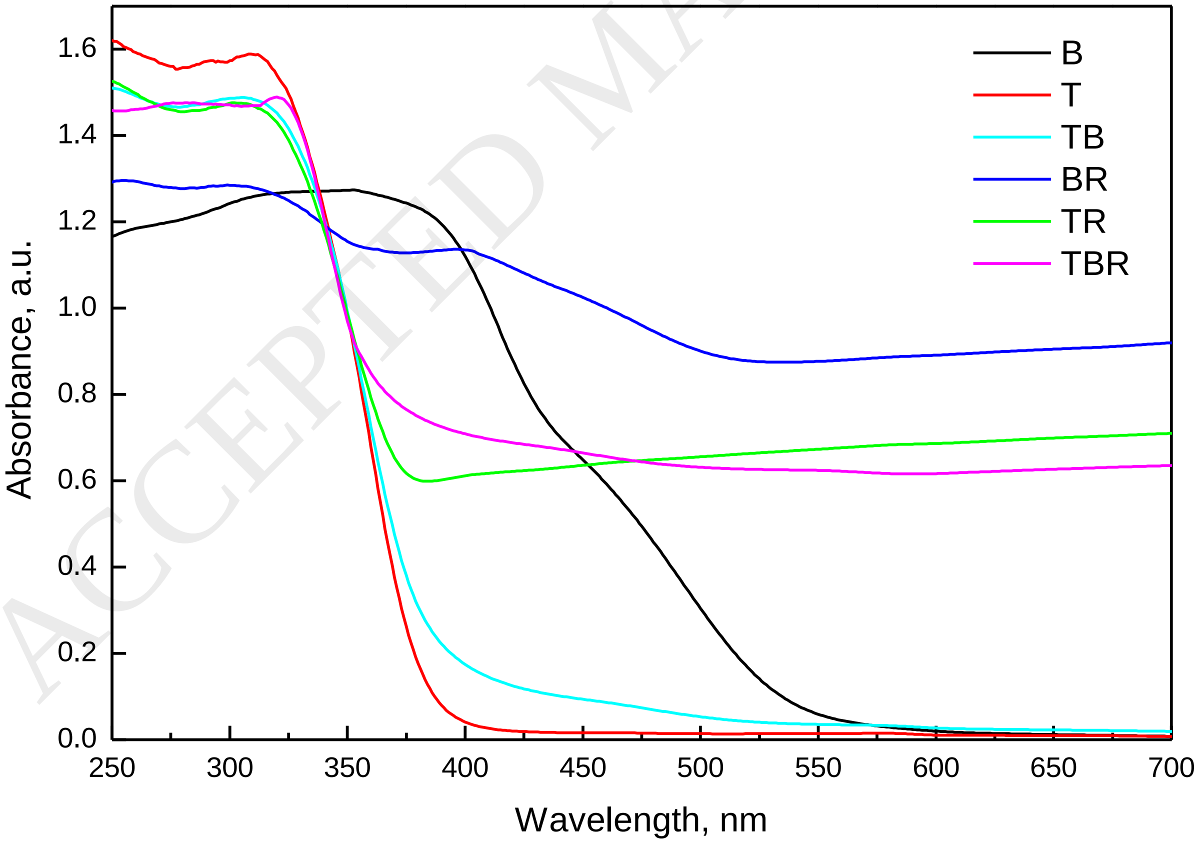

Fig. 6. UV-Vis DR spectra of synthesized catalysts.

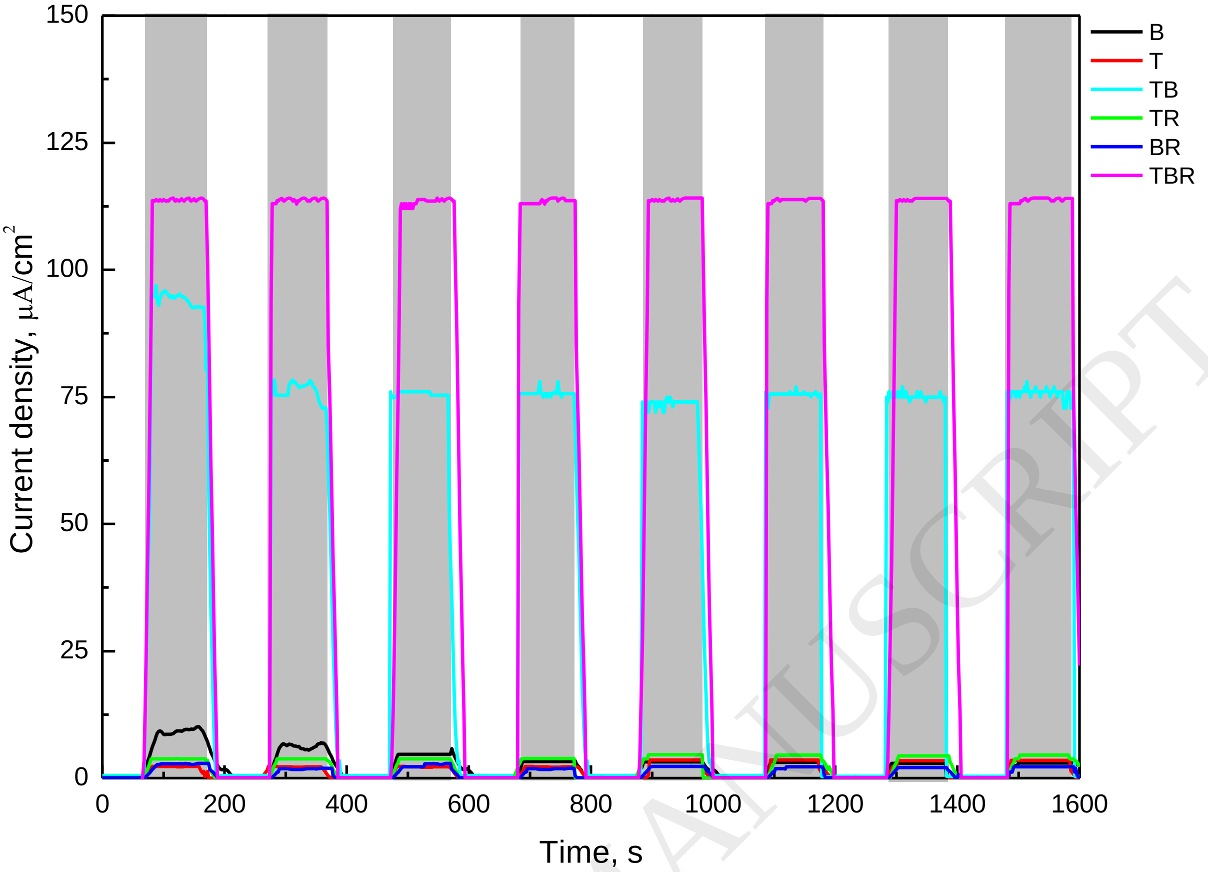

Fig. 7. Photocurrent at photoelectrode (powder solids were deposited onto the graphene working electrode) measured under intermittent visible light (halogen lamp 150 W, λ_{max} = 520 nm, UV cut off filter at 410 nm, grey area) irradiation in KOH (0.1 M).

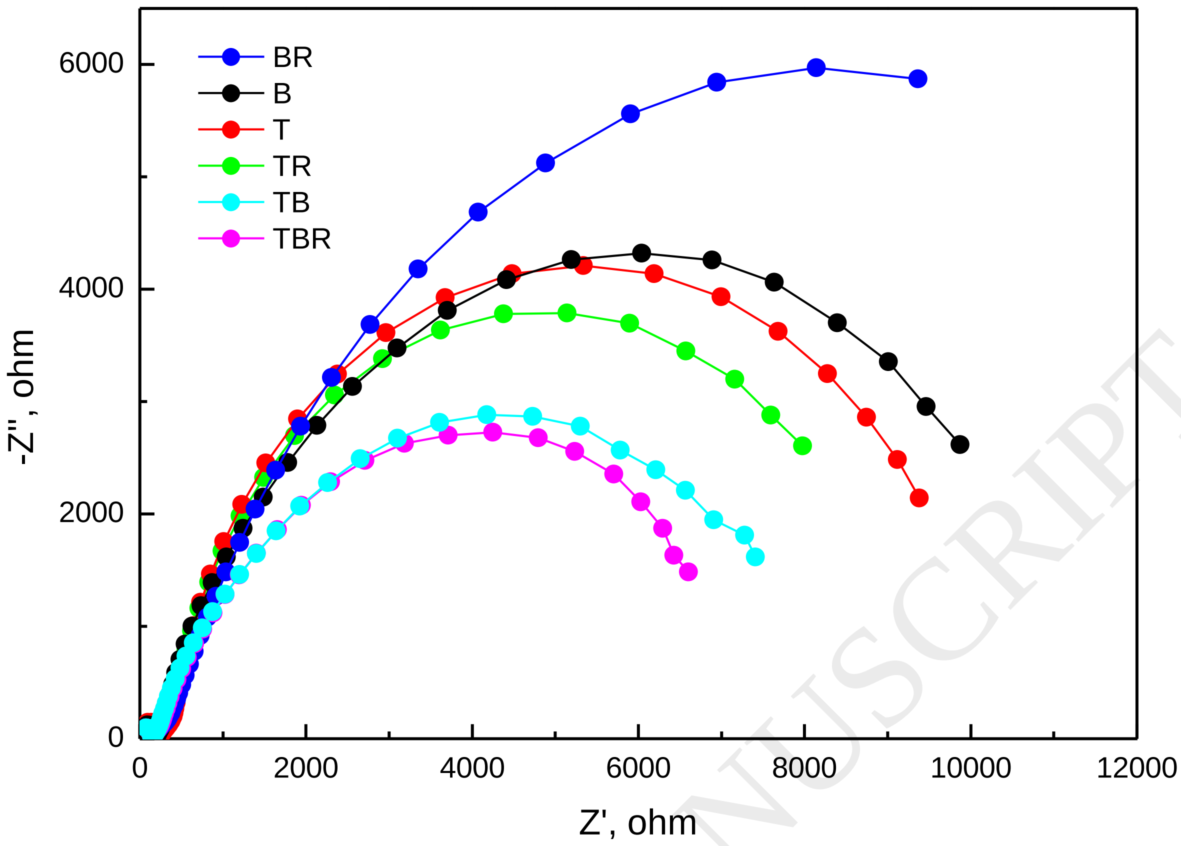

Fig. 8. Electrochemical impedance spectra of prepared catalysts under visible light illumination.

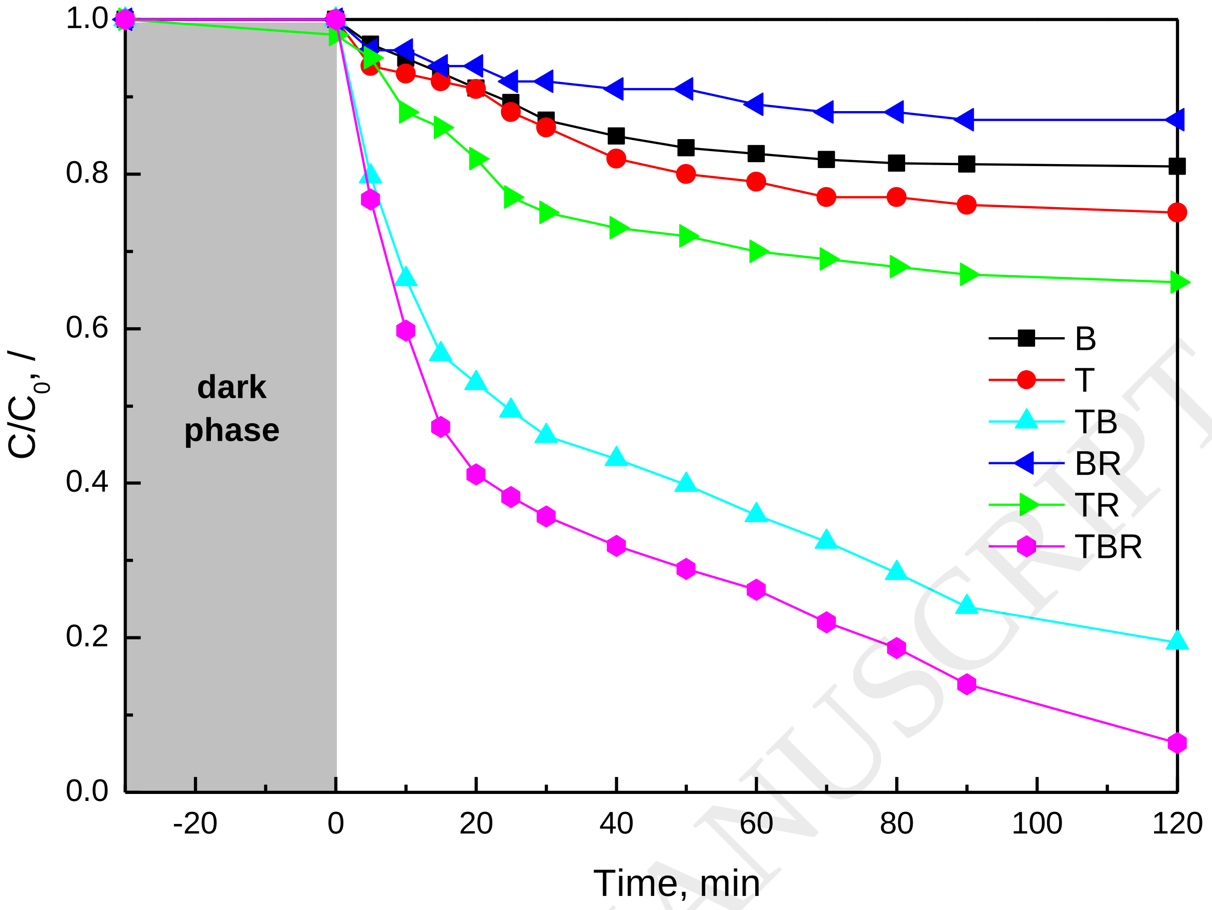

Fig. 9. Photocatalytic degradation of BPA in the presence of prepared catalysts irradiated with visible light (halogen lamp 150 W, λ_{max}= 520 nm, UV cut off filter at 410 nm). The catalyst concentration used in the performed experiments was 125 mg/l.

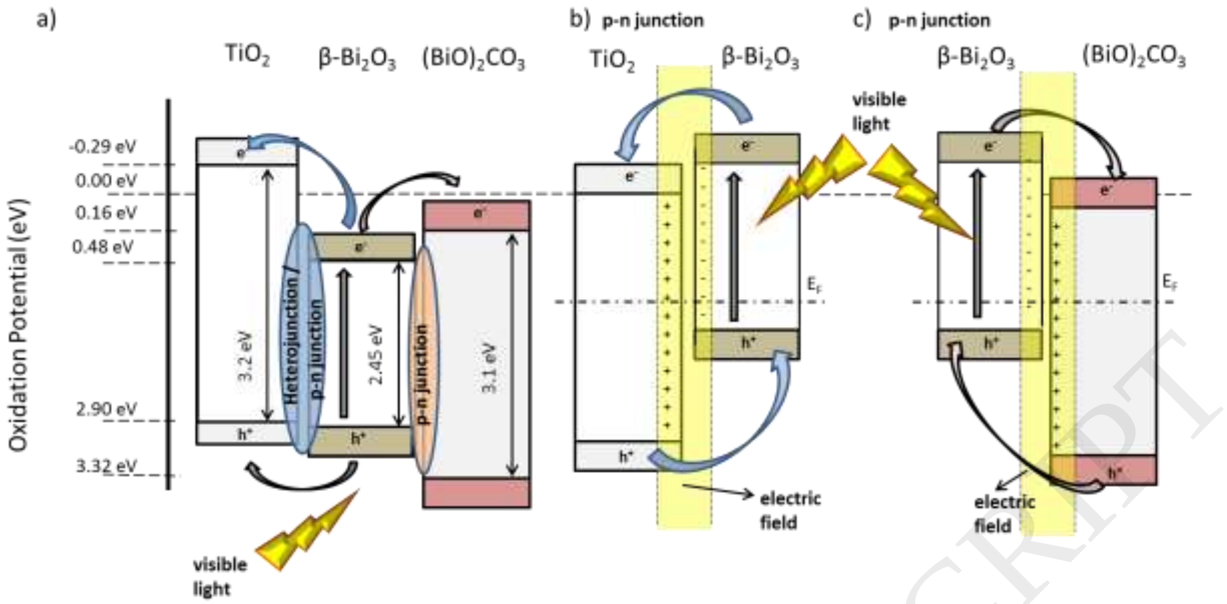

Fig. 10. a) Graphical illustration of a plausible charge carrier migration cascade in TB composite, b) formation of the TiO_2/β-Bi_2O_3 p-n junction and the possible charge separation process, and c) formation of the β-Bi_2O_3/$(BiO)_2CO_3$ p-n junction and the possible charge separation process.

Table 1. BET specific surface area (S_{BET}), total pore volume (V_{pore}), average pore diameter (d_{pore}) and average anatase TiO_2 crystallite size of synthesized catalysts.

Sample	S_{BET} (m^2/g)	V_{pore} (cm^3/g)	d_{pore} (nm)	Average crystallite size (nm)
B	4.7	0.02	16.5	30*
T	105	0.57	19.3	14°
TB	80.6	0.40	17.5	15°, N.D.*, 18**
BR	20.4	0.07	11.9	45*, 16**
TR	108	0.48	15.5	16°
TBR	89.8	0.35	13.5	15°, N.D.*, N.D.**

°Average crystallite size of anatase TiO_2 (JCPDS 00-021-1272).

*Average crystallite size of tetragonal β-Bi_2O_3 (JCPDS 00-027-0050).

**Average crystallite size of $(BiO)_2CO_3$ (JCPDS 00-041-1488).

N.D. = not determined.

Table 2. Carbon content accumulated on the surface of composite catalysts before (TC_{fresh}) and after (TC_{spent}) photocatalytic BPA degradation. TOC removal (TOC_R) combined with true TOC conversion (TOC_m) and TOC accumulation (TOC_a).

Sample	TOC_R	TC_{fresh}	TC_{spent}	TC_{spent}-TC_{fresh}	TOC_m	TOC_a
	(%)	(wt. %)			(%)	
T	11	0.23	0.68	0.45	4	7
TB	51	0.36	0.87	0.51	43	8
B	4	0.34	0.5	0.26	1.4	2.6
TBR	60	/	/	/	/	/
BR	0	/	/	/	/	/
TR	6	/	/	/	/	/